

MODELS OF NEPTUNE-MASS EXOPLANETS: EMERGENT FLUXES AND ALBEDOS

DAVID S. SPIEGEL¹, ADAM BURROWS¹, LAURENT IBGUI¹, IVAN HUBENY², JOHN A. MILSOM³¹Department of Astrophysical Sciences, Princeton University, Peyton Hall, Princeton, NJ 08544²Steward Observatory, The University of Arizona, Tucson, AZ 85721 and³Department of Physics, The University of Arizona, Tucson, AZ 85721*Submitted to ApJ*

ABSTRACT

There are now many known exoplanets with $M \sin i$ within a factor of two of Neptune's, including the transiting planets GJ436b and HAT-P-11b. Planets in this mass-range are different from their more massive cousins in several ways that are relevant to their radiative properties and thermal structures. By analogy with Neptune and Uranus, they are likely to have metal abundances that are an order of magnitude or more greater than those of larger, more massive planets. This increases their opacity, decreases Rayleigh scattering, and changes their equation of state. Furthermore, their smaller radii mean that fluxes from these planets are roughly an order of magnitude lower than those of otherwise identical gas giant planets. Here, we compute a range of plausible radiative equilibrium models of GJ436b and HAT-P-11b. In addition, we explore the dependence of generic Neptune-mass planets on a range of physical properties, including their distance from their host stars, their metallicity, the spectral type of their stars, the redistribution of heat in their atmospheres, and the possible presence of additional optical opacity in their upper atmospheres.

Subject headings: equation of state – line: profiles – planetary systems – radiative transfer
– stars: individual GJ436, HAT-P-11 – astrochemistry

1. INTRODUCTION

Although in the early days of exoplanet research large, massive planets (gas giants) were discovered in disproportionate numbers, lower mass objects, including super Earths (1 to ~ 10 times the mass of the Earth) and ice-giants, are now being found with increasing frequency.¹ The latter population, consisting of “Neptune-mass” bodies (those with masses within a factor of a few of Neptune's), currently numbers several dozen, and is growing rapidly.

Exoplanet transits, first observed by Henry et al. (2000) and Charbonneau et al. (2000), allow precise measurements both of planet masses (by breaking the degeneracy between mass and inclination angle) and of radii. These two crucial pieces of data provide constraints on models of structure, evolution, and bulk composition (Ibgui & Burrows 2009; Burrows et al. 2007a, 2000; Guillot 2008, 2005; Guillot & Showman 2002; Baraffe et al. 2005). As a result, the best-studied among the Neptune-mass population are the transiting planets GJ436b (1.33 times the mass of Neptune, and 1.27 times its radius; Caceres et al. 2009; Bean & Seifahrt 2008; Bean et al. 2008; Torres 2007; Deming et al. 2007a; Maness

et al. 2007) and HAT-P-11b ($1.50M_{\text{Nep}}$, $1.30R_{\text{Nep}}$; Bakos et al. 2009; Dittman et al. 2009).

Observations of an exoplanet can constrain theoretical models. The marriage of data with theory, therefore, allows us to learn about the physical conditions on these distant worlds. For example, observations during transit can constrain various properties, including both the atmospheric composition and structure at the terminator (Seager & Sasselov 2000; Hubbard et al. 2001; Charbonneau et al. 2002; Désert et al. 2008; Redfield et al. 2008) and the motion of the atmosphere (Brown 2001; Spiegel et al. 2007). This paper, however, focuses on the diagnostics of planetary structure that are available from observations of a planet's disk, not of its limb. The disks of those planets whose orbits are aligned precisely enough that they transit may be studied in exquisite detail. Half an orbit after transit, they undergo secondary eclipse, when they pass behind their host stars. Immediately before and after secondary eclipse, a planet is in its “full-moon” phase, when its reflected and emitted light are at their maximum from our vantage. There have been a variety of ground-based and space-based secondary-eclipse observations of exoplanets in the last several years (Richardson et al. 2003; Snellen 2005; Deming et al. 2007a,b; Charbonneau et al. 2008; Knutson et al. 2008, 2009; Alonso et al. 2009b,a; Sing & López-Morales 2009). In the last decade, several

Electronic address: dsp@astro.princeton.edu, burrows@astro.princeton.edu, ibgui@astro.princeton.edu, hubeny@as.arizona.edu, milsom@physics.arizona.edu

¹ See the catalog at <http://exoplanet.eu>.

groups have produced a progression of theoretical models of the atmospheres of Jupiter-mass exoplanets (Sudarsky et al. 2000, 2003; Hubeny et al. 2003; Burrows et al. 2005; Fortney et al. 2006; Burrows et al. 2008a; Fortney et al. 2008; Burrows et al. 2008b; Spiegel et al. 2009; Showman et al. 2009), including calculations of both optical albedos and infrared emergent spectra. These calculations are now being used in interpretative studies of the secondary eclipse observations.²

A critical difference between the gas giant and the ice-giant planets motivates the present investigation of theoretical models of lower mass objects. The gas giants of our solar system – Jupiter and Saturn – have metal abundances not more than a few times solar (Matter et al. 2009; Saumon & Guillot 2004). However, Neptune, Uranus, and, presumably, extrasolar planets in the same mass-range, are thought to have bulk metallicities of 30–45 times solar (Figueira et al. 2009; Matter et al. 2009; Guillot & Gautier 2007). Increased metallicity leads to increased opacity. Reduced relative hydrogen abundance might also reduce the importance of Rayleigh scattering in the atmospheres of Neptune-mass planets.

In the last several years, infrared observations by the *Spitzer Space Telescope*, in conjunction with theoretical models by our group and others, have suggested that several giant planets have thermal inversions, wherein, above a relative minimum, the atmospheric temperature increases with altitude. Hubeny et al. (2003) suggested that, if there is an additional source of upper atmosphere optical opacity, incident stellar irradiation could lead to precisely this type of atmospheric structure. The planets whose emergent spectra have suggested thermal inversions include HD 209458b (Burrows et al. 2007b; Knutson et al. 2008), HD 149026b (Fortney et al. 2006; Burrows et al. 2008a), TrES-4 (Knutson et al. 2009), XO-1b (Machalek et al. 2008), XO-2b (Machalek et al. 2009), XO-3b (McCullough et al. 2008), and, perhaps, *v* Andromeda b (Burrows et al. 2008a). Various authors have suggested that titanium oxide (TiO), as a strong optical absorber, might provide the extra opacity that is needed to produce the inferred inversions (Fortney et al. 2008; Showman et al. 2009). However, Spiegel et al. (2009) argue that, without extremely vigorous macroscopic mixing, a heavy molecule such as TiO will settle to a level that is too deep for it to contribute to an inversion. Furthermore, Spiegel et al. (2009) show that several planets for which inversions have been inferred ought to have cold-trap regions deeper in their atmospheres that are cool enough for titanium to condense and rain out, therefore requiring even more vigorous mixing if TiO is to survive up to the millibar levels where

² Comparable calculations have been made in the context of Super-Earth planets (Miller-Ricci et al. 2009; Kaltenecker et al. 2009).

it would be needed.³ Zahnle et al. (2009) suggest that sulfur photochemistry provides another avenue for achieving the additional upper-atmosphere optical opacity that is needed to produce inversions. The ultimate cause of inversions remains unknown, and might differ from one planet to another. Nevertheless, sources of extra optical opacity might be related to metal abundance, and so it is reasonable to wonder whether some highly irradiated Neptune-mass planets might have thermal inversions.

In order to survey the range of plausible structures of Neptune-mass exoplanets, we compute a variety of model atmospheres. We explore how the emergent infrared fluxes and optical albedos of GJ436b and HAT-P-11b depend both on the redistribution of heat in their atmospheres and on the possible presence of an extra source of atmospheric opacity (following the treatment in Burrows et al. 2008a and Spiegel et al. 2009). We also examine how “ice-giant” atmospheres, and their optical and infrared fluxes, depend on their distances from their host stars, their atmospheric metal abundances, and the spectral types of their hosts. By “ice-giant,” we are simply referring to a planet with approximately Neptune’s mass and radius; whether the atmosphere is bounded below by ices is irrelevant to our analysis. Our models are of planets with hydrogen/helium-dominated atmospheres that are metal-enriched relative to solar by a large factor. We note that some planets currently classified as “Super-Earths” might share this structure.

The remainder of this paper is structured as follows: In §2, we present our numerical techniques for computing the atmospheres of “ice-giant” planets. In §3, we describe the different models that we ran. Section 4 contains the results of our calculations. Finally, in §5, we summarize our findings.

2. NUMERICAL METHODS

We calculate radiative equilibrium models of irradiated planetary atmospheres models. As in our other recent studies, we use the code `COOLTLUSTY` (Hubeny et al. 2003; Sudarsky et al. 2003; Burrows et al. 2006, 2008a; Spiegel et al. 2009). This code is an variant of the code `TLUSTY` (Hubeny 1988; Hubeny & Lanz 1995), with atomic and molecular opacities appropriate to the cooler environments of planetary atmospheres and brown dwarfs (Sharp & Burrows 2007; Burrows & Sharp 1999; Burrows et al. 2001, augmented by Burrows et al. 2002 and Burrows et al. 2005). Irradiation in planetary atmosphere models is incorporated using Kurucz model stellar spectra, interpolated to the temperatures and surface gravities appropriate to our study (Kurucz 1979, 1994, 2005).

In order to examine the effect of metallicity on

³ The analysis of Showman et al. 2009 appears to agree with this conclusion.

planet atmospheres, we compute some models with solar abundance of metals, and others with $30\times$ solar abundance. For both metallicities, we derive the chemical equilibrium abundances (as functions of temperature and density) of several hundred atomic and molecular species (Sharp & Burrows 2007). Using chemical equilibrium abundances, we calculate the monochromatic opacities that are used in the radiative transfer calculations. Furthermore, we recompute the equation of state tables for the chemical abundances derived for $30\times$ solar metallicity.

To treat the redistribution of incident stellar flux in a planet’s atmosphere, we use the P_n formalism described in Burrows et al. (2006) and Burrows et al. (2008a). In this formalism, in lieu of calculating the full three dimensional general circulation, the proportion of day-side incident flux that is transported to and reradiated from the night-side is parameterized as P_n , which plausibly ranges between 0, corresponding to all stellar flux being instantaneously reradiated, and 0.5, corresponding to the night side receiving approximately the same amount of stellar energy as the dayside (as a result of advective heat redistribution). The redistribution takes place between 0.003 bars and 0.6 bars.

For each model planet, we calculate the temperature-pressure profile, the planet-star flux ratio of emergent infrared radiation, the optical albedo, and the temperature and pressure, as functions of wavelength, of the $\tau_\lambda = 2/3$ photosphere. It is worthwhile to note that, since photons are not stamped as being reflected/scattered stellar photons or emitted photons that arose in a planet’s atmosphere, the albedo is simply the quotient of emergent flux with incident flux (Burrows et al. 2008b; Sudarsky et al. 2003, 2000). Defined this way, it is in principle possible for albedos to be greater than 1.⁴ However, at wavelengths shorter than $1\ \mu\text{m}$, the albedos we report may be understood as being predominantly measures of reflectance and scattering properties of the day-side atmospheres.

3. PLANET MODELS

The known exoplanets in Neptune’s mass range are found in a variety of configurations. Table 1 summarizes their diversity. Orbital separations range from 0.02 AU to 2.7 AU, and stellar types from M through G are represented. The diversity of observed planet-star systems motivates our investigation of a comparably diverse model set.

Our goal in this investigation is twofold: (*i*) to examine the diagnostics of the known transiting extrasolar “ice-giants” (GJ436b and HAT-P-11b); and (*ii*) to examine more generally the types of radiative and thermal structures that might obtain in plausible exo-Neptunian atmospheres. To these ends, we

⁴ In fact, this happens in the mid-infrared, where planets are strong thermal emitters.

compute 29 model atmospheres, listed in Table 2.^{5,6}

Six of the models of GJ436b are named T35a03Z01P0k0G through T35a03Z01P5k0G (corresponding to a GJ436b-like planet around a GJ436-like star, with P_n ranging between 0.0 and 0.5).⁷ Two additional models are T35a03Z01P3k2G (corresponding to GJ436b with $P_n = 0.3$ and an additional optical absorber of opacity $\kappa = 0.2\ \text{cm}^2\ \text{g}^{-1}$ in the upper atmosphere, where κ is the same as κ_e from Burrows et al. 2008a) and T35a03Z30P0k0G (corresponding to GJ436b with $P_n = 0.0$ and no extra optical absorber, and with opacity corresponding to $30\times$ solar metallicity). As in previous work, κ is gray over the range 3×10^{14} - 7×10^{14} Hz. The models of HAT-P-11b are T48a05Z01P0k0H through T48a05Z01P5k0H (HAT-P-11b with P_n ranging from 0.0 to 0.5) and T48a05Z01P3k2H (extra upper atmosphere absorber of opacity $\kappa = 0.2\ \text{cm}^2\ \text{g}^{-1}$). The additional optical opacity in models T35a03Z01P3k2G and T48a05Z01P3k2H is confined to the pressure range from ~ 5 mbar to the top of the atmosphere.

We also test more generic “ice-giant” models, broadly sampling a wide range of possible conditions. In particular, we test the effect of orbital separation, of metallicity, and of stellar type. OGLE-05-169L-b, at 2.7 AU, is a bit of an outlier and will not be observed in the near future. The remainder of the known Neptune-mass exoplanets are predominantly at separations $a \lesssim 0.5$ AU. This motivates our decision to examine planets in this range of separations in this initial study. Models testing the effects of orbital separation and of metallicity are T58a03Z01P1k0G through T58a50Z01P1k0G (solar metallicity models from 0.03 AU to 0.50 AU around a sun-like star), and T58a03Z30P1k0G through T58a50Z30P1k0G ($30\times$ solar metallicity, at the same distances from the same star). Models testing the effect of stellar type are T35a03Z01P1k0G through T62a03Z01P1k0G. These models place a GJ436b-size planet at 0.03 AU from, respectively, GJ436 ($T = 3500$ K, $\log_{10} g = 4.80$), an M0V star ($T = 4200$ K, $\log_{10} g = 4.70$), HAT-P-11 ($T = 4780$ K, $\log_{10} g = 4.60$), a KOV star ($T = 5200$ K, $\log_{10} g = 4.50$), a sun-like star ($T = 5778$ K, $\log_{10} g = 4.44$), and an F9V star ($T = 6200$ K, $\log_{10} g = 4.25$).

⁵ There are 31 rows in Table 2, of which two, the 26th and 30th are duplicates.

⁶ These models are publicly available at <http://www.astro.princeton.edu/~dsp/exoneptunes/> and at <http://www.astro.princeton.edu/~burrows/>.

⁷ In this labeling convention, the symbols have the following meanings: “T”, for temperature, is followed by 0.01 times the star’s effective temperature; “a”, for semimajor axis, is followed by 100 times the orbital semimajor axis in AU; “Z”, for metallicity, is followed by the ratio with respect to solar abundance of metals; “P” is followed by 10 times P_n ; “k” is followed by 10 times κ (in $\text{cm}^2\ \text{g}^{-1}$); the final letter (“G” or “H”) indicates whether the radius and surface gravity of the model planet match those of GJ436b or HAT-P-11b.

4. RESULTS

For each model planet, we present two observable variables and three that are not observable. The observables are the emergent infrared flux, presented as a planet-star flux ratio, and the optical albedo. The three variables that are unobservable, but are nonetheless useful probes of our models, are the following: the temperature-pressure profile (temperature as a function of depth in the atmosphere); the temperature, as a function of wavelength, of the $\tau_\lambda = 2/3$ photosphere; and the pressure, as a function of wavelength, of the same photosphere.

4.1. *GJ436b and HAT-P-11b*

The most salient difference between GJ436b and HAT-P-11b is that the latter orbits a hotter, brighter star. The temperature-pressure profiles of models of them, portrayed in Fig. 1, reflect this: HAT-P-11b (bottom panel of Fig. 1) is consistently hotter at a given pressure. For both profiles, the redistribution of day-side irradiation to the night side reduces the dayside’s temperature. As P_n increases, the thermal profile becomes cooler at a given pressure in the range where the redistribution takes place (0.003 bars to 0.6 bars in these models). This effect is more pronounced in GJ436b than in HAT-P-11b.

On the other hand, the effect of an additional optical absorber (green curves, $\kappa = 0.2 \text{ cm}^2 \text{ g}^{-1}$) is more pronounced in HAT-P-11b’s profile – precisely because its star is hotter and, therefore, brighter in the optical. In GJ436b’s model, an additional optical absorber at high altitude increases upper atmosphere temperatures by a modest $\sim 60 \text{ K}$. In HAT-P-11b’s model, however, an extra optical absorber increases the temperature at $\sim 10^{-3}$ bars by $\sim 300 \text{ K}$, and creates a thermal inversion of about 100 K .

In the figure for GJ436b, we have included one additional model (T35a03Z01P0k0G), with $P_n = 0.0$ and $30\times$ solar opacity. The profile of this model looks qualitatively different from those of the other models, because it does not quite extend to the marginally-stable convection zone. However, the Rosseland mean optical depth at the base of this model is ~ 80 , and the net flux is constant with altitude, so the unmodeled portions of the atmosphere do not affect the emergent spectrum.

Let us consider our four wavelength-dependent model diagnostics, presented in Fig. 2 (GJ436b) and Fig. 3 (HAT-P-11b). We have smoothed the curves in each plot to a spectral resolution of 100 for ease in viewing. In the flux-ratio plot of Fig. 2 (upper left panel), we include the $8\text{-}\mu\text{m}$ measurement that Deming et al. (2007a) obtained with the *Spitzer* InfraRed Array Camera (IRAC).

The models’ emergent infrared fluxes show var-

ious spectral features. The opacity database contains significant CH_4 cross section at $3.3 \mu\text{m}$ and $7.8 \mu\text{m}$, H_2O and CO absorption at $4.5 \mu\text{m}$, and H_2O at $6 \mu\text{m}$ and $10 \mu\text{m}$ (Sharp & Burrows 2007). The emergent flux is insensitive to P_n at some wavelengths, and shows a moderate-to-strong dependence on P_n at others (stronger in the models of GJ436b than in those of HAT-P-11b). The effect of increasing P_n is to reduce the emergent flux in “emission” features, specifically at $\sim 4 \mu\text{m}$, $\sim 5 \mu\text{m}$, $\sim 6.5 \mu\text{m}$, and $\sim 10\text{-}15 \mu\text{m}$.

The optical albedo (upper right panels of both figures) does not exhibit a strong dependence on P_n . At wavelengths shorter than $0.5 \mu\text{m}$, the albedo is nonnegligible, due to Rayleigh scattering. At longer wavelengths, it tends to be $\lesssim 0.05$. In both figures, the albedos of models with $\kappa = 0.0 \text{ cm}^2 \text{ g}^{-1}$ start to increase longward of $\sim 0.8 \mu\text{m}$. Albedos of HAT-P-11b models are somewhat higher at these wavelengths. Note, for both models, the dip in optical albedo at $\sim 0.95 \mu\text{m}$, which is due to a water absorption feature (Sharp & Burrows 2007).

Although the temperature and pressure of the $\tau_\lambda = 2/3$ photosphere are not observable (bottom left and right panels, respectively), it is instructive to examine the effect of increasing P_n on these variables. When $P_n = 0.0$, the temperature varies significantly with wavelength, as narrow windows of low opacity allow flux from the deeper, warmer portions of the atmosphere to escape. As P_n increases, the location of the photosphere becomes more nearly constant with wavelength. The pressure of the photosphere does not vary much with P_n , except near $5 \mu\text{m}$. As seen in the bottom right panel, most of the infrared spectrum originates at pressures between 10^{-3} and 0.1 bars. For these pressures, as seen in the upper left panel, the day-side energy sink for $P_n = 0.5$ (and to a lesser extent for lower P_n ’s) decreases the T gradient so that for $P_n = 0.5$ there is a quasi-plateau in temperature plateau these pressures.

The effect of an added source of opacity in the high atmosphere has striking consequences for both the emergent flux and albedo. Although models T35a03Z01P0k0G through T35a03Z01P5k0G ($\kappa = 0.0 \text{ cm}^2 \text{ g}^{-1}$) all produce lower planet flux at $8 \mu\text{m}$ than Deming et al. (2007a) measured, model T35a03Z01P3k2G ($\kappa = 0.2 \text{ cm}^2 \text{ g}^{-1}$) has an IRAC-bandpass-integrated $8\text{-}\mu\text{m}$ flux that is more than 20% higher than that of T35a03Z01P3k0G (the $P_n = 0.3$ model with no extra optical absorber), and is closer to being consistent with the data point’s error bars.⁸ Furthermore, model T35a03Z30P0k0G, with zero redistribution and $30\times$ solar opacity, has an integrated $8\text{-}\mu\text{m}$ flux that is 7.5% higher than that of the analogous model with solar opacity. Still, its $8\text{-}\mu\text{m}$ flux is 12% lower than bottom of

⁸ A model with $\kappa = 0.5 \text{ cm}^2 \text{ g}^{-1}$ (not shown) passes right through the center of the error bars.

the 1- σ range on the Deming et al. (2007a) measurement. In both models T35a03Z01P3k2G and T48a05Z01P3k2H (GJ436b and HAT-P-11b with $\kappa = 0.2 \text{ cm}^2 \text{ g}^{-1}$), an extra optical absorber causes the upper atmosphere to be warmer and the planet flux and the photospheric temperature to show fewer spectra features. Despite the warmer upper atmosphere temperatures and generally warmer photospheres, however, the additional optical opacity causes the the albedo to be much lower in the optical ($\lesssim 0.01$ throughout much of the optical) because Rayleigh scattering is diminished. This is the case even though the thermal component of emission is greater by dint of the higher temperature.⁹

Consider again the flux-ratio comparisons for GJ436b (upper left panels of Fig. 2). All 8 models have approximately the same flux at 4.6 μm , but flux varies significantly at 4.0 μm . The ratio of the planet's flux at 4.0 μm to that at 4.6 μm varies from ~ 2.4 for T35a03Z01P0k0G to ~ 1.2 for T35a03Z01P4k0G and T35a03Z01P3k2G to ~ 0.8 for T35a03Z01P5k0G. Similarly, the ratio of flux at $\sim 10 \mu\text{m}$ to flux at 4.6 μm provides a constraint on the redistribution of heat. This ratio varies from ~ 7.6 for T35a03Z01P0k0G to ~ 4.5 for T35a03Z01P5k0G. These flux ratios, therefore, could provide a handle on the amount of redistribution of heat. In addition, at 7 to 8 μm , extra upper atmosphere opacity (T35a03Z01P3k2G) increases the emergent flux to $\sim 20\%$ above what it would be without the extra absorber. We note that the difference between the 30 \times solar opacity model and those with solar opacity appears greater when one considers the full spectral shape than when integrated over the 8- μm IRAC band.

The models of HAT-P-11b exhibit a qualitatively analogous dependence on P_n , although the ratios are quantitatively somewhat different because of the differences between the two stars and the two orbital separations. But, again, T48a05Z01P0k0H has significantly greater flux at 4.0 μm (by a factor of ~ 2) and at 10 μm (by a factor of ~ 1.4) than T48a05Z01P5k0H. Furthermore, because HAT-P-11b is a hotter star with correspondingly more of its flux in the optical, an extra optical absorber in the upper atmosphere has a more significant effect on this planet than on GJ436b. Between 7-8 μm , T48a05Z01P3k2H is approximately twice as bright as the models without an extra absorber, and is also much brighter (by $\sim 40\%$) at wavelengths greater than 15 μm .

4.2. Distance

The temperature of an irradiated stellar companion's photosphere drops off rapidly with increas-

ing orbital separation, and its emergent flux decreases correspondingly. For separations greater than $\sim 0.5 \text{ AU}$, both the reflected/scattered optical light and the infrared emission become too dim to be detected without spatially separating (and masking) the light of the star. Although direct detection of wide-separation Neptune-mass objects will be feasible in the future (Burrows 2005), in this paper we focus on objects within 0.5 AU of their primaries.

The top panel of Fig. 4 presents temperature-pressure profiles of models at 0.03, 0.05, 0.10, 0.30, and 0.50 AU from a sun-like star (G2V). In these models (T58a03Z01P0k0G through T58a50Z30P0k0G in Table 2), $\kappa = 0.0 \text{ cm}^2 \text{ g}^{-1}$ and $P_n = 0.0$. Solar opacity models are represented by solid curves, and 30 \times solar opacity models with dashed curves; the differences between these are discussed in §4.3 below.

Figure 5 contains four panels analogous to the four of Fig. 3. The predominant trends with distance in the flux-ratio plot (upper left panel) and in the photospheric temperature plot (lower left panel) are, respectively, that both the planet flux and planet temperature decrease as the model planet is moved farther from the star. In addition, there is some change in the spectral shape – cooler, more distant planets have redder spectra. The albedos of these models (upper right panel of Fig. 5) change from low at short wavelengths and high (~ 0.7) at long wavelengths for the 0.03 AU models to moderate (~ 0.3) at short wavelengths and low at long wavelengths for the 0.50 AU models. The close-in models have relatively high apparent albedo at wavelengths approaching 1 μm because of the contribution from the Wien tails of their thermal emission.

4.3. Metallicity

It was initially surprising to us that models with higher metallicity around solar-type stars, with their concomitant changes in both opacity and equation of state, nevertheless have extremely similar spectral profiles to their lower metallicity cousins (solid and dashed lines in top left panel of Fig. 5). The temperature-pressure profiles (top panel of Fig. 4) of 30 \times solar opacity models are quite different from those of solar opacity models; increasing metallicity appears to translate the T - P profiles up to higher altitudes (lower pressures). But the photospheric temperature (bottom panel of Fig. 5) remains essentially unchanged with higher opacity.

How is this possible? The photosphere pressure plot (lower right panel of Fig. 5) offers the explanation. Because, viewed from the outside, the optical depth increases so much more quickly with depth into atmosphere for the high metallicity models, their $\tau_\lambda = 2/3$ surfaces are at significantly lower pressures (by roughly an order of magnitude), cor-

⁹ At sufficiently high values of κ and with sufficient irradiation, this trend would reverse, and higher κ would lead to a larger apparent albedo.

responding to much higher altitudes. But, as Fig. 4 shows, higher in the atmosphere the temperature is higher in the high metallicity models, and these two effects conspire to leave the temperature of the photospheres of the high metallicity models virtually unchanged (bottom left panel of Fig. 5).

The changes to the albedos (top right panels of Fig. 5) are not dramatic, although at the short wavelength end the albedos of the 30×solar metallicity models are about half that of the solar metallicity models. Furthermore, at the long wavelength end, a deep absorption feature due to water arises at $\sim 0.95 \mu\text{m}$ in the high metallicity models that is not present in the low metallicity ones. Since the two characteristics that are significantly different at high metallicity (the T - P profile and the photospheric pressure) are not observable, these comparatively modest changes to albedo might represent our best chance to constrain the atmospheric metallicity through whole-disk observations (though transit spectrum observations could provide a complementary constraint). Note, however, that this water feature is the same one seen in solar metallicity models of GJ436b and HAT-P-11b in Figs. 2 and 3, and, therefore, might be a signature of high metallicity only in the context of a modeling effort that includes the appropriate stellar irradiance spectrum.

For a solar-type irradiation spectrum, the opacity (solar or 30× solar) of model planet’s atmosphere has a minor influence on the emergent spectrum. However, the opacity has a stronger influence when the irradiation spectrum is from a cool M-dwarf (as shown in Fig. 2, where the irradiation is from GJ436).

4.4. Stellar Type

How do a Neptune-mass planet’s structure and appearance depend on its host star? Models T35a03Z01P0k0G through T62a03Z01P0k0G address this question. These models are of planets the size of GJ436b, separated 0.029 AU from stars ranging from cool (3500 K) to moderately hot (6200 K).

The most prominent differences between models around cooler and dimmer stars and those around hotter stars is that, unsurprisingly, planets around hotter stars are hotter and bluer. The bottom panel of Fig. 4 and the bottom left panel of Fig. 6 indicate how more massive, brighter stars lead to hotter planets at a given distance.

For a planetary system that is of order a Gyr or older, a Neptune-mass planet has lost almost all of its heat of formation (Burrows et al. 2000, 2003; Baraffe et al. 2005). As a result, for planets at separations ≤ 0.5 AU, contributions to the emergent planetary flux (reflected/scattered and emitted) from self-luminance are miniscule. Therefore, the integrated planet flux divided by the integrated stellar flux is, to a high degree of approximation,

simply $1/(4\pi)$ times the solid angle subtended by the planet from the vantage of the star ($\Omega_p/4\pi = \pi R_p^2/4\pi a^2$). This leads to the somewhat counter-intuitive flux-ratios plot in the upper left corner of Fig. 6: in the mid-infrared (at wavelengths greater than $\sim 8 \mu\text{m}$), a planet around a cool star is significantly brighter relative to its star than one around a hot star. Of course, this is because the same total relative flux is distributed predominantly at longer wavelengths for a cooler planet and at shorter wavelengths for a hotter planet.

Interestingly, at wavelengths less than $\sim 8 \mu\text{m}$, the photospheric pressures are not dramatically different for the six models, despite very different T - P profiles. Finally, similar to the trend seen in albedo versus distance seen in §4.2, cooler models have higher albedos at short wavelengths, while hotter models have higher apparent albedos at longer wavelengths as the Wien tail enters into the optical and near infrared.

5. SUMMARY AND CONCLUSIONS

We have presented a series of theoretical 1-D models of the radiative and thermal structures of Neptune-mass, “ice-giant” exoplanets, including models at opacities corresponding both to solar metallicity and to 30×solar. To produce the latter, we computed equilibrium chemical abundances of hundreds of molecular and atomic species, and we recomputed the equation of state with the higher mean molecular weight. We produced models of the transiting planets GJ436b and HAT-P-11b, and models of generic planets in a range of plausible conditions.

In our investigation of GJ436b and HAT-P-11b, we find the following:

- The ratio of planet flux at $4.0 \mu\text{m}$ or at $10 \mu\text{m}$ to that at $4.6 \mu\text{m}$ might place a constraint on the amount of redistribution of heat from the day to the night side: more redistribution leads to a smaller flux ratio. The ratio of planet flux at $7 \mu\text{m}$ to that at $4.6 \mu\text{m}$ might place a constraint on the possible presence of an extra optical absorber in the high atmosphere.
- An extra optical absorber, if present in either planet, would have a more dramatic effect on both the T - P profile and the emergent spectrum of HAT-P-11b than of GJ436b, because HAT-P-11 is brighter in the optical.
- Models of GJ436b without an extra absorber are significantly dimmer than the Deming et al. (2007a) measurement, while the model with an extra absorber of opacity $\kappa = 0.2 \text{ cm}^2 \text{ g}^{-1}$ is closer to being consistent with the measurement, though still shy of it.

- Models of these two planets have moderate optical albedos (~ 0.3) at the short wavelength end of the spectrum, and low albedos at longer wavelengths.

Furthermore, we find the following broad trends among generic models of planets in this mass-range:

- Higher metallicity implies higher opacity for a given column mass of atmosphere. As a result, photospheres of higher metallicity models are at lower pressures.
- Nonetheless, when the irradiation spectrum is from a solar-type star, higher metallicity models appear to differ little from solar metallicity models in observable variables. The most noticeable difference, among close-in planets around solar-type stars, is the water absorption feature at $\sim 0.95 \mu\text{m}$ that shows up in higher metallicity models. When the irradiation spectrum is from a cool M-dwarf (GJ436), the metallicity of the planet's atmosphere has a larger influence on the emergent spectrum.
- Neptune-mass planets around cooler stars have larger flux ratios in the mid-infrared than ones at the same distance around hotter stars.

(This conclusion is germane to Jupiter-mass planets, as well.)

Close-in Neptune-mass planets present an observational challenge because, with radii a factor of ~ 3 smaller than Jupiter-mass planets, they are roughly an order of magnitude dimmer. However, observations of GJ436b have already been made with *Spitzer*, and additional ones are planned. For GJ436b, 3.6 and 4.5 μm IRAC observations will help to quantify both the amount of redistribution of heat from the day to the night sides and the possible presence of an extra absorber in the high atmosphere. Future observations with new facilities will provide constraints on models of other planets in this mass range, and will sharpen our understanding of this class of objects.

We thank Jason Nordhaus, Nikole Lewis, and Adam Showman for helpful discussions. We thank our anonymous referee for a number of helpful comments that improved the manuscript. This study was supported in part by NASA grant NNX07AG80G. We also acknowledge support through JPL/Spitzer Agreements 1328092, 1348668, and 1312647.

REFERENCES

- Alonso, R., Alapini, A., Aigrain, S., Auvergne, M., Baglin, A., Barbieri, M., Barge, P., Bonomo, A. S., Borde, P., Bouchy, F., Chaintreuil, S., De la Reza, R., Deeg, H. J., Deleuil, M., Dvorak, R., Erikson, A., Fridlund, M., Fialho, F., Gondoin, P., Guillot, T., Hatzes, A., Jorda, L., Lammer, H., Leger, A., Llebaria, A., Magain, P., Mazeh, T., Moutou, C., Ollivier, M., Patzold, M., Pont, F., Queloz, D., Rauer, H., Rouan, D., Schneider, J., & Wuchterl, G. 2009a, ArXiv e-prints
- Alonso, R., Guillot, T., Mazeh, T., Aigrain, S., Alapini, A., Barge, P., Hatzes, A., & Pont, F. 2009b, ArXiv e-prints
- Bakos, G. Á., Torres, G., Pál, A., Hartman, J., Kovács, G., Noyes, R. W., Latham, D. W., Sasselov, D. D., Sipőcz, B., Esquerdo, G. A., Fischer, D. A., Johnson, J. A., Marcy, G. W., Butler, R. P., Isaacson, H., Howard, A., Vogt, S., Kovács, G., Fernandez, J., Moór, A., Stefanik, R. P., Lázár, J., Papp, I., & Sári, P. 2009, ArXiv e-prints
- Baraffe, I., Chabrier, G., Barman, T. S., Selsis, F., Allard, F., & Hauschildt, P. H. 2005, A&A, 436, L47
- Bean, J. L., Benedict, G. F., Charbonneau, D., Homeier, D., Taylor, D. C., McArthur, B., Seifahrt, A., Dreizler, S., & Reiners, A. 2008, A&A, 486, 1039
- Bean, J. L. & Seifahrt, A. 2008, A&A, 487, L25
- Bonfils, X., Mayor, M., Delfosse, X., Forveille, T., Gillon, M., Perrier, C., Udry, S., Bouchy, F., Lovis, C., Pepe, F., Queloz, D., Santos, N. C., & Bertaux, J.-L. 2007, A&A, 474, 293
- Bouchy, F., Moutou, C., & Queloz, D. 2009, in CoRoT International Symposium I
- Brown, T. M. 2001, ApJ, 553, 1006
- Burrows, A. 2005, Nature, 433, 261
- Burrows, A., Budaj, J., & Hubeny, I. 2008a, ApJ, 678, 1436
- Burrows, A., Dulick, M., Bauschlicher, Jr., C. W., Bernath, P. F., Ram, R. S., Sharp, C. M., & Milsom, J. A. 2005, ApJ, 624, 988
- Burrows, A., Guillot, T., Hubbard, W. B., Marley, M. S., Saumon, D., Lunine, J. I., & Sudarsky, D. 2000, ApJ, 534, L97
- Burrows, A., Hubbard, W. B., Lunine, J. I., & Liebert, J. 2001, Reviews of Modern Physics, 73, 719
- Burrows, A., Hubeny, I., Budaj, J., & Hubbard, W. B. 2007a, ApJ, 661, 502
- Burrows, A., Hubeny, I., Budaj, J., Knutson, H. A., & Charbonneau, D. 2007b, ApJ, 668, L171
- Burrows, A., Ibgui, L., & Hubeny, I. 2008b, ApJ, 682, 1277
- Burrows, A., Ram, R. S., Bernath, P., Sharp, C. M., & Milsom, J. A. 2002, ApJ, 577, 986
- Burrows, A. & Sharp, C. M. 1999, ApJ, 512, 843
- Burrows, A., Sudarsky, D., & Hubbard, W. B. 2003, ApJ, 594, 545
- Burrows, A., Sudarsky, D., & Hubeny, I. 2006, ApJ, 650, 1140
- Caceres, C., Ivanov, V. D., Minniti, D., Naef, D., Melo, C., Mason, E., Selman, F., & Pietrzynski, G. 2009, ArXiv e-prints
- Charbonneau, D., Brown, T. M., Latham, D. W., & Mayor, M. 2000, ApJ, 529, L45
- Charbonneau, D., Brown, T. M., Noyes, R. W., & Gilliland, R. L. 2002, ApJ, 568, 377
- Charbonneau, D., Knutson, H. A., Barman, T., Allen, L. E., Mayor, M., Megeath, S. T., Queloz, D., & Udry, S. 2008, ApJ, 686, 1341
- Deming, D., Harrington, J., Laughlin, G., Seager, S., Navarro, S. B., Bowman, W. C., & Horning, K. 2007a, ApJ, 667, L199
- Deming, D., Richardson, L. J., & Harrington, J. 2007b, MNRAS, 378, 148
- Désert, J.-M., Vidal-Madjar, A., Lecavelier Des Etangs, A., Sing, D., Ehrenreich, D., Hébrard, G., & Ferlet, R. 2008, A&A, 492, 585

- Dittman, J. A., Close, L. M., Green, E. M., Scuderi, L. J., & Males, J. R. 2009, ArXiv e-prints
- Figueira, P., Pont, F., Mordasini, C., Alibert, Y., Georgy, C., & Benz, W. 2009, *A&A*, 493, 671
- Fischer, D. A., Marcy, G. W., Butler, R. P., Vogt, S. S., Laughlin, G., Henry, G. W., Abouav, D., Peek, K. M. G., Wright, J. T., Johnson, J. A., McCarthy, C., & Isaacson, H. 2008, *ApJ*, 675, 790
- Fortney, J. J., Cooper, C. S., Showman, A. P., Marley, M. S., & Freedman, R. S. 2006, *ApJ*, 652, 746
- Fortney, J. J., Lodders, K., Marley, M. S., & Freedman, R. S. 2008, *ApJ*, 678, 1419
- Forveille, T., Bonfils, X., Delfosse, X., Gillon, M., Udry, S., Bouchy, F., Lovis, C., Mayor, M., Pepe, F., Perrier, C., Queloz, D., Santos, N., & Bertaux, J.-L. 2009, The HARPS search for southern extra-solar planets
- Fressin, F., Aigrain, S., Charbonneau, D., Fridlund, M., Guillot, T., Knutson, H., Mazeh, T., Pont, F., Rauer, H., & Torres, G. 2009, in *Spitzer Proposal ID #534*, 534+
- Gould, A., Udalski, A., An, D., Bennett, D. P., Zhou, A.-Y., Dong, S., Rattenbury, N. J., Gaudi, B. S., Yock, P. C. M., Bond, I. A., Christie, G. W., Horne, K., Anderson, J., Stanek, K. Z., DePoy, D. L., Han, C., McCormick, J., Park, B.-G., Pogge, R. W., Poindexter, S. D., Soszyński, I., Szymański, M. K., Kubiak, M., Pietrzyński, G., Szewczyk, O., Wyrzykowski, L., Ulaczyk, K., Paczyński, B., Bramich, D. M., Snodgrass, C., Steele, I. A., Burgdorf, M. J., Bode, M. F., Botzler, C. S., Mao, S., & Swaving, S. C. 2006, *ApJ*, 644, L37
- Guillot, T. 2005, *Annual Review of Earth and Planetary Sciences*, 33, 493
- 2008, *Physica Scripta Volume T*, 130, 014023
- Guillot, T. & Gautier, D. 2007, *Treatise on Geophysics, Planets and Moons*, vol. 10 (Elsevier, Amsterdam)
- Guillot, T. & Showman, A. P. 2002, *A&A*, 385, 156
- Henry, G. W., Marcy, G. W., Butler, R. P., & Vogt, S. S. 2000, *ApJ*, 529, L41
- Howard, A. W., Johnson, J. A., Marcy, G. W., Fischer, D. A., Wright, J. T., Henry, G. W., Giguere, M. J., Isaacson, H., Valenti, J. A., Anderson, J., & Piskunov, N. E. 2009, *The Astrophysical Journal*, 696, 75
- Hubbard, W. B., Fortney, J. J., Lunine, J. I., Burrows, A., Sudarsky, D., & Pinto, P. 2001, *ApJ*, 560, 413
- Hubeny, I. 1988, *Computer Physics Communications*, 52, 103
- Hubeny, I., Burrows, A., & Sudarsky, D. 2003, *ApJ*, 594, 1011
- Hubeny, I. & Lanz, T. 1995, *ApJ*, 439, 875
- Ibgui, L. & Burrows, A. 2009, *ApJ*, 700, 1921
- Kaltenegger, L., Selsis, F., Fridlund, M., Lammer, H., Beichman, C., Danchi, W., Eiroa, C., Henning, T., Herbst, T., Leger, A., Liseau, R., Lunine, J., Paresce, F., Penny, A., Quirrenbach, A., Roettgering, H., Schneider, J., Stam, D., Tinetti, G., & White, G. J. 2009, ArXiv e-prints
- Knutson, H. A., Charbonneau, D., Allen, L. E., Burrows, A., & Megeath, S. T. 2008, *ApJ*, 673, 526
- Knutson, H. A., Charbonneau, D., Burrows, A., O'Donovan, F. T., & Mandushev, G. 2009, *ApJ*, 691, 866
- Kurucz, R. 1994, *Solar abundance model atmospheres for 0.1,2,4,8 km/s. Kurucz CD-ROM No. 19*. Cambridge, Mass.: Smithsonian Astrophysical Observatory, 1994., 19
- Kurucz, R. L. 1979, *ApJS*, 40, 1
- 2005, *Memorie della Societa Astronomica Italiana Supplement*, 8, 14
- Lovis, C., Mayor, M., Pepe, F., Alibert, Y., Benz, W., Bouchy, F., Correia, A. C. M., Laskar, J., Mordasini, C., Queloz, D., Santos, N. C., Udry, S., Bertaux, J.-L., & Sivan, J.-P. 2006, *Nature*, 441, 305
- Machalek, P., McCullough, P. R., Burke, C. J., Valenti, J. A., Burrows, A., & Hora, J. L. 2008, *ApJ*, 684, 1427
- Machalek, P., McCullough, P. R., Burrows, A., Burke, C. J., Hora, J. L., & Johns-Krull, C. M. 2009, *ApJ*, 701, 514
- Maness, H. L., Marcy, G. W., Ford, E. B., Hauschildt, P. H., Shreve, A. T., Basri, G. B., Butler, R. P., & Vogt, S. S. 2007, *PASP*, 119, 90
- Marcy, G., Butler, R. P., Fischer, D., Vogt, S., Wright, J. T., Tinney, C. G., & Jones, H. R. A. 2005, *Progress of Theoretical Physics Supplement*, 158, 24
- Matter, A., Guillot, T., & Morbidelli, A. 2009, *Planet. Space Sci.*, 57, 816
- Mayor, M., Bonfils, X., Forveille, T., Delfosse, X., Udry, S., Bertaux, J., Beust, H., Bouchy, F., Lovis, C., Pepe, F., Perrier, C., Queloz, D., & Santos, N. C. 2009, ArXiv e-prints
- Mayor, M., Udry, S., Lovis, C., Pepe, F., Queloz, D., Benz, W., Bertaux, J.-L., Bouchy, F., Mordasini, C., & Segransan, D. 2009, *A&A*, 493, 639
- McCullough, P., Burke, C., Burrows, A., Hora, J., Johns-Krull, C., & Machalek, P. 2008, in *Spitzer Proposal ID #525*, 525+
- Melo, C., Santos, N. C., Gieren, W., Pietrzyński, G., Ruiz, M. T., Sousa, S. G., Bouchy, F., Lovis, C., Mayor, M., Pepe, F., Queloz, D., da Silva, R., & Udry, S. 2007, *A&A*, 467, 721
- Miller-Ricci, E., Seager, S., & Sasselov, D. 2009, *ApJ*, 690, 1056
- O'Toole, S., Tinney, C. G., Butler, R. P., Jones, H. R. A., Bailey, J., Carter, B. D., Vogt, S. S., Laughlin, G., & Rivera, E. J. 2009a, *ApJ*, 697, 1263
- O'Toole, S. J., Jones, H. R. A., Tinney, C. G., Butler, R. P., Marcy, G. W., Carter, B., Bailey, J., & Wittenmyer, R. A. 2009b, ArXiv e-prints
- Pepe, F., Correia, A. C. M., Mayor, M., Tamuz, O., Couetdic, J., Benz, W., Bertaux, J.-L., Bouchy, F., Laskar, J., Lovis, C., Naef, D., Queloz, D., Santos, N. C., Sivan, J.-P., Sosnowska, D., & Udry, S. 2007, *A&A*, 462, 719
- Poveda, A. & Lara, P. 2008, in *Revista Mexicana de Astronomia y Astrofisica*, vol. 27, Vol. 34, *Revista Mexicana de Astronomia y Astrofisica Conference Series*, 49–52
- Redfield, S., Endl, M., Cochran, W. D., & Koesterke, L. 2008, *ApJ*, 673, L87
- Richardson, L. J., Deming, D., & Seager, S. 2003, *ApJ*, 597, 581
- Saumon, D. & Guillot, T. 2004, *ApJ*, 609, 1170
- Seager, S. & Sasselov, D. D. 2000, *ApJ*, 537, 916
- Sharp, C. M. & Burrows, A. 2007, *ApJS*, 168, 140
- Showman, A. P., Fortney, J. J., Lian, Y., Marley, M. S., Freedman, R. S., Knutson, H. A., & Charbonneau, D. 2009, *ApJ*, 699, 564
- Sing, D. K. & López-Morales, M. 2009, *A&A*, 493, L31
- Snellen, I. A. G. 2005, *MNRAS*, 363, 211
- Spiegel, D. S., Haiman, Z., & Gaudi, B. S. 2007, *ApJ*, 669, 1324
- Spiegel, D. S., Silverio, K., & Burrows, A. 2009, *ApJ*, 699, 1487
- Sudarsky, D., Burrows, A., & Hubeny, I. 2003, *ApJ*, 588, 1121
- Sudarsky, D., Burrows, A., & Pinto, P. 2000, *ApJ*, 538, 885
- Torres, G. 2007, *ApJ*, 671, L65
- Vogt, S. S., Butler, R. P., Marcy, G. W., Fischer, D. A., Henry, G. W., Laughlin, G., Wright, J. T., & Johnson, J. A. 2005, *ApJ*, 632, 638
- Wright, J. T., Marcy, G. W., Fischer, D. A., Butler, R. P., Vogt, S. S., Tinney, C. G., Jones, H. R. A., Carter, B. D., Johnson, J. A., McCarthy, C., & Apps, K. 2007, *ApJ*, 657, 533
- Wright, J. T., Upadhyay, S., Marcy, G. W., Fischer, D. A., Ford, E. B., & Johnson, J. A. 2009, *ApJ*, 693, 1084
- Zahnle, K., Marley, M. S., Freedman, R. S., Lodders, K., & Fortney, J. J. 2009, *ApJ*, 701, L20

TABLE 1
CHARACTERISTICS OF \sim NEPTUNE-MASS EXOPLANETS

Planet	Mass ($M_{\text{Nep}}^{\text{a}}$)	Radius ($R_{\text{Nep}}^{\text{b}}$)	$\log_{10} g$ (cgs)	Semi-major Axis (AU)	Stellar Type	References
CoRoT-7b	0.65	0.43	3.59	0.02	K0 V	Fressin et al. 2009
GJ436b	1.33	1.04	3.15	0.03	M2.5	Torres 2007
HAT-P-11b	1.50	3.05	1.22	0.05	K4	Bakos et al. 2009 Dittman et al. 2009
HD 181433b	0.44	-	-	0.08	K3 IV	Bouchy et al. 2009
HD 285968b	0.49	-	-	0.07	M2.5 V	Forveille et al. 2009
HD 40307d	0.53	-	-	0.13	K2.5 V	Mayor et al. 2009
HD 7924b	0.54	-	-	0.06	K0 V	Howard et al. 2009
HD 69830b	0.61	-	-	0.08	K0 V	Lovis et al. 2006
HD 160691c	0.62	-	-	0.09	G3 IV-V	Pepe et al. 2007
55 Cnc e	0.63	-	-	0.04	G8 V	Poveda & Lara 2008
GJ 674b	0.69	-	-	0.04	M2.5	Bonfils et al. 2007
HD 69830c	0.70	-	-	0.19	K0 V	Lovis et al. 2006
OGLE-05-169L b	0.74	-	-	~ 2.7	-	Gould et al. 2006
HD 4308b	0.87	-	-	0.11	G5 V	O'Toole et al. 2009b
GJ 581b	0.91	-	-	0.04	M3	Mayor et al. 2009
HD 190360c	1.06	-	-	0.13	G6 IV	Vogt et al. 2005
HD 69830d	1.08	-	-	0.63	K0 V	Lovis et al. 2006
HD 219828b	1.22	-	-	0.05	G0 IV	Melo et al. 2007
HD 16417b	1.28	-	-	0.14	G1 V	O'Toole et al. 2009a
HD 47186b	1.33	-	-	0.05	G5 V	Bouchy et al. 2009
HD 99492b	2.02	-	-	0.12	K2 V	Marcy et al. 2005
HD 11964b	2.04	-	-	0.23	G5	Wright et al. 2009
HD 49674b	2.13	-	-	0.06	G5 V	Wright et al. 2007
55 Cnc f	2.67	-	-	0.78	G8 V	Fischer et al. 2008

^aThe mass of Neptune is $M_{\text{Nep}} = 1.02 \times 10^{33}$ g = $0.054 M_{\text{Jup}}$, where $M_{\text{Jup}} = 1.90 \times 10^{33}$ g.

^bThe radius of Neptune is $R_{\text{Nep}} = 2.48 \times 10^9$ cm = $0.346 R_{\text{Jup}}$, where $R_{\text{Jup}} = 7.15 \times 10^9$ cm.

TABLE 2
EXOPLANET MODELS^a

Model Name	Stellar Model	a (AU)	Metallicity (Z_{\odot})	P_n	R_p (R_{Nep})	$\log_{10} g$ (cgs)	κ ($\text{cm}^2 \text{g}^{-1}$)
T35a03Z01P0k0G	GJ436 ($T = 3500 \text{ K}$; $\log_{10} g = 4.80$)	0.03	1	0.0	1.04	3.145	0.0
T35a03Z01P1k0G	GJ436 ($T = 3500 \text{ K}$; $\log_{10} g = 4.80$)	0.03	1	0.1	1.04	3.145	0.0
T35a03Z01P2k0G	GJ436 ($T = 3500 \text{ K}$; $\log_{10} g = 4.80$)	0.03	1	0.2	1.04	3.145	0.0
T35a03Z01P3k0G	GJ436 ($T = 3500 \text{ K}$; $\log_{10} g = 4.80$)	0.03	1	0.3	1.04	3.145	0.0
T35a03Z01P4k0G	GJ436 ($T = 3500 \text{ K}$; $\log_{10} g = 4.80$)	0.03	1	0.4	1.04	3.145	0.0
T35a03Z01P5k0G	GJ436 ($T = 3500 \text{ K}$; $\log_{10} g = 4.80$)	0.03	1	0.5	1.04	3.145	0.0
T48a05Z01P0k0H	HAT-P-11 ($T = 4780 \text{ K}$; $\log_{10} g = 4.60$)	0.05	1	0.0	1.22	3.052	0.0
T48a05Z01P1k0H	HAT-P-11 ($T = 4780 \text{ K}$; $\log_{10} g = 4.60$)	0.05	1	0.1	1.22	3.052	0.0
T48a05Z01P2k0H	HAT-P-11 ($T = 4780 \text{ K}$; $\log_{10} g = 4.60$)	0.05	1	0.2	1.22	3.052	0.0
T48a05Z01P3k0H	HAT-P-11 ($T = 4780 \text{ K}$; $\log_{10} g = 4.60$)	0.05	1	0.3	1.22	3.052	0.0
T48a05Z01P4k0H	HAT-P-11 ($T = 4780 \text{ K}$; $\log_{10} g = 4.60$)	0.05	1	0.4	1.22	3.052	0.0
T48a05Z01P5k0H	HAT-P-11 ($T = 4780 \text{ K}$; $\log_{10} g = 4.60$)	0.05	1	0.5	1.22	3.052	0.0
T35a03Z01P3k2G	GJ436 ($T = 3500 \text{ K}$; $\log_{10} g = 4.80$)	0.03	1	0.3	1.04	3.145	0.2
T48a05Z01P3k2H	HAT-P-11 ($T = 4780 \text{ K}$; $\log_{10} g = 4.60$)	0.05	1	0.3	1.22	3.052	0.2
T35a03Z30P0k0G	GJ436 ($T = 3500 \text{ K}$; $\log_{10} g = 4.80$)	0.03	30	0.0	1.04	3.145	0.0
T58a03Z01P0k0G	G2 V ($T = 5778 \text{ K}$; $\log_{10} g = 4.44$)	0.03	1	0.0	1.04	3.145	0.0
T58a05Z01P0k0G	G2 V ($T = 5778 \text{ K}$; $\log_{10} g = 4.44$)	0.05	1	0.0	1.04	3.145	0.0
T58a10Z01P0k0G	G2 V ($T = 5778 \text{ K}$; $\log_{10} g = 4.44$)	0.10	1	0.0	1.04	3.145	0.0
T58a25Z01P0k0G	G2 V ($T = 5778 \text{ K}$; $\log_{10} g = 4.44$)	0.25	1	0.0	1.04	3.145	0.0
T58a50Z01P0k0G	G2 V ($T = 5778 \text{ K}$; $\log_{10} g = 4.44$)	0.50	1	0.0	1.04	3.145	0.0
T58a03Z30P0k0G	G2 V ($T = 5778 \text{ K}$; $\log_{10} g = 4.44$)	0.03	30	0.0	1.04	3.145	0.0
T58a05Z30P0k0G	G2 V ($T = 5778 \text{ K}$; $\log_{10} g = 4.44$)	0.05	30	0.0	1.04	3.145	0.0
T58a10Z30P0k0G	G2 V ($T = 5778 \text{ K}$; $\log_{10} g = 4.44$)	0.10	30	0.0	1.04	3.145	0.0
T58a25Z30P0k0G	G2 V ($T = 5778 \text{ K}$; $\log_{10} g = 4.44$)	0.25	30	0.0	1.04	3.145	0.0
T58a50Z30P0k0G	G2 V ($T = 5778 \text{ K}$; $\log_{10} g = 4.44$)	0.50	30	0.0	1.04	3.145	0.0
T35a03Z01P0k0G ^b	GJ436 ($T = 3500 \text{ K}$; $\log_{10} g = 4.80$)	0.03	1	0.0	1.04	3.145	0.0
T42a03Z01P0k0G	M0 V ($T = 4200 \text{ K}$; $\log_{10} g = 4.70$)	0.03	1	0.0	1.04	3.145	0.0
T48a03Z01P0k0G	HAT-P-11 ($T = 4780 \text{ K}$; $\log_{10} g = 4.60$)	0.03	1	0.0	1.04	3.145	0.0
T52a03Z01P0k0G	K0 V ($T = 5200 \text{ K}$; $\log_{10} g = 4.50$)	0.03	1	0.0	1.04	3.145	0.0
T58a03Z01P0k0G ^c	G2 V ($T = 5778 \text{ K}$; $\log_{10} g = 4.44$)	0.03	1	0.0	1.04	3.145	0.0
T62a03Z01P0k0G	F9 V ($T = 6200 \text{ K}$; $\log_{10} g = 4.25$)	0.03	1	0.0	1.04	3.145	0.0

This table contains 31 rows describing the 29 models we computed. Two rows are repeated.

^aThe model name is a shorthand for the model characteristics, as follows: “T” is for temperature, followed by the temperature in Kelvin divided by 100; “a” is for semimajor axis, followed by 10 times the orbital separation in AU; “Z” is for metallicity, followed by the multiple of solar abundance; “P” is for P_n , followed by $10 \times P_n$; “k” is for κ , followed by $10 \times \kappa$ (in $\text{cm}^2 \text{g}^{-1}$). The final letter is either “G” or “H”: if “G”, the planet’s radius and surface gravity are those of GJ436b; if “H”, they are those of HAT-P-11b.

^bThis is a repeat of the first row.

^cThis is a repeat of the 15th row.

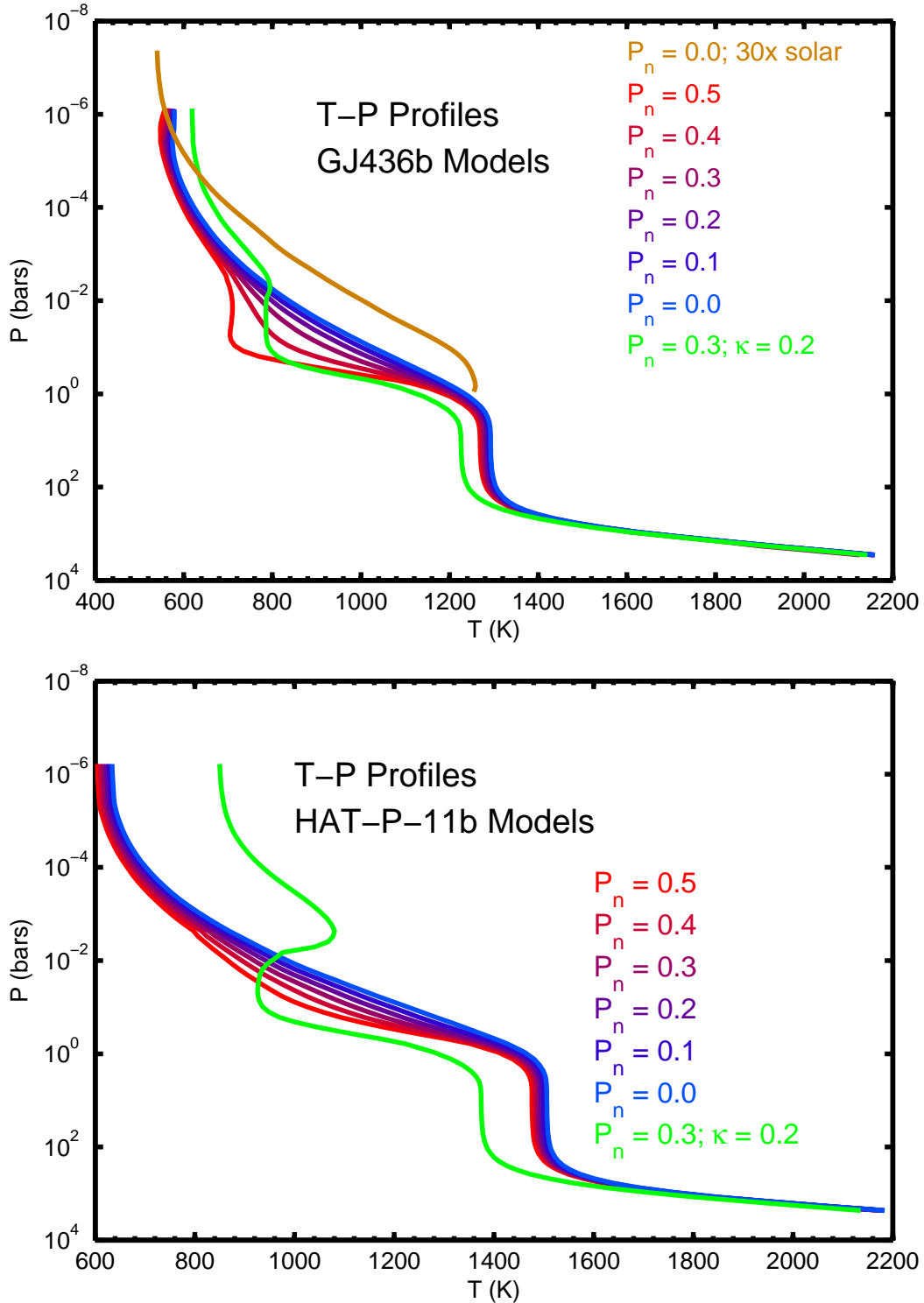


FIG. 1.— Model temperature-pressure profiles of GJ436b and HAT-P-11 b. *Top*: Models of GJ436b, with the redistribution parameter P_n varying from 0 (no redistribution) to 0.5 (complete redistribution of heat to the night side). A model is shown with added upper atmosphere opacity $\kappa = 0.2 \text{ cm}^2 \text{ g}^{-1}$ (here, κ is the same as the κ_e from Burrows et al. 2008a). An additional model shows the influence of 30x solar atmospheric opacity. *Bottom*: Same, for HAT-P-11 b, except without the 30x solar model.

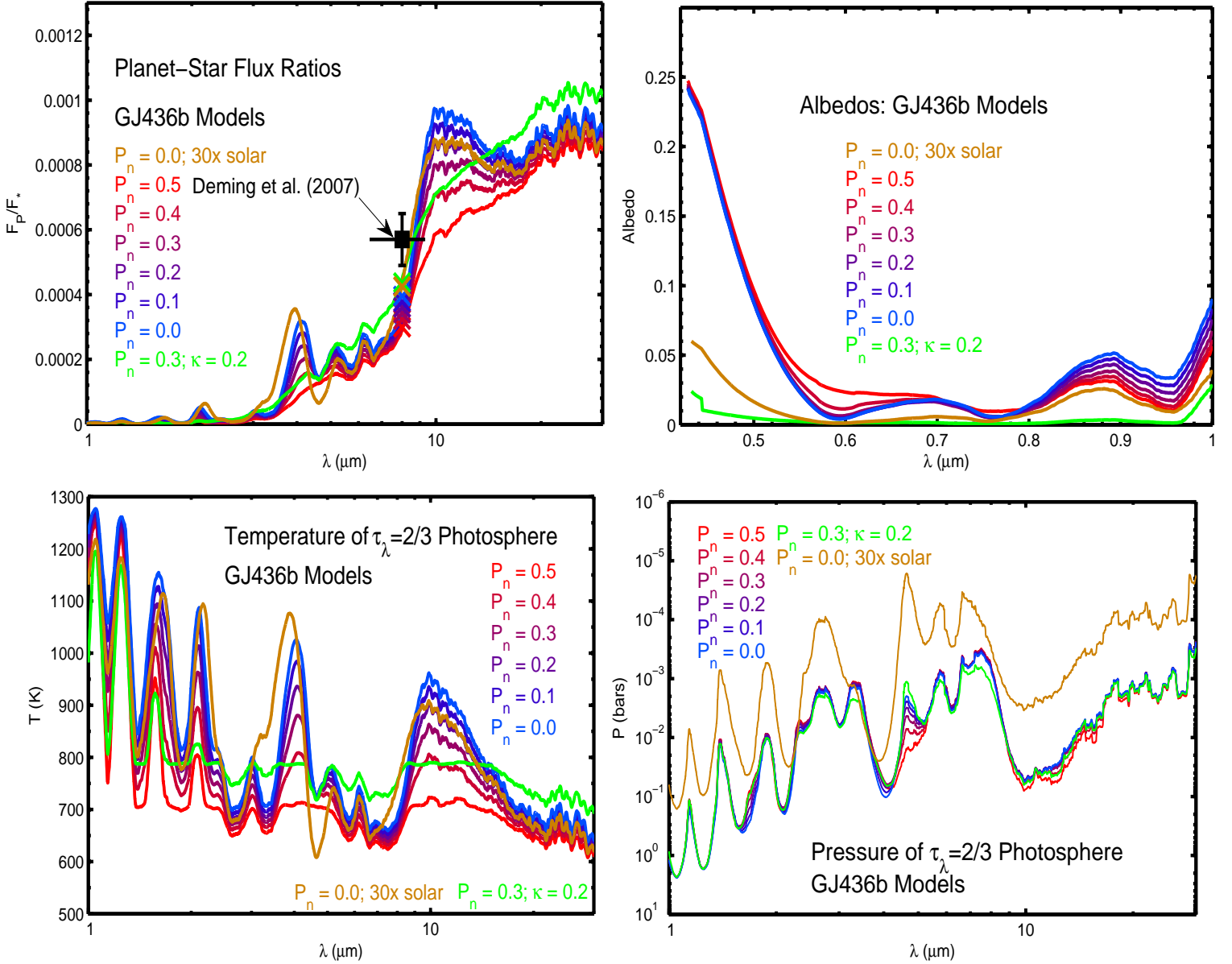


FIG. 2.— Additional characteristics of models of GJ436b depicted in the top panel of Fig. 1. *Top left*: Planet-star flux ratios. Varying P_n has little influence on the planet’s flux at $8 \mu\text{m}$, but an additional upper atmosphere absorber results in a significantly better match of the model to the data. 30 \times solar atmospheric opacity also helps bridge the gap between the solar-opacity models and the observed data. The black square is the *Spitzer* IRAC-4 measurement of Deming et al. (2007a); vertical bars indicate $1\text{-}\sigma$ uncertainty; the horizontal bar indicates the full width at 10% maximum of the IRAC-4 band’s transmission function. Large X’s indicate integrated planet flux divided by integrated stellar flux over this band. *Top right*: Albedos. The albedo is lower for lower P_n , and much lower for nonzero κ . *Bottom left*: Temperature of the $\tau_{\lambda} = 2/3$ surface, as a function of wavelength. *Bottom right*: Pressure of the $\tau_{\lambda} = 2/3$ surface, as a function of wavelength.

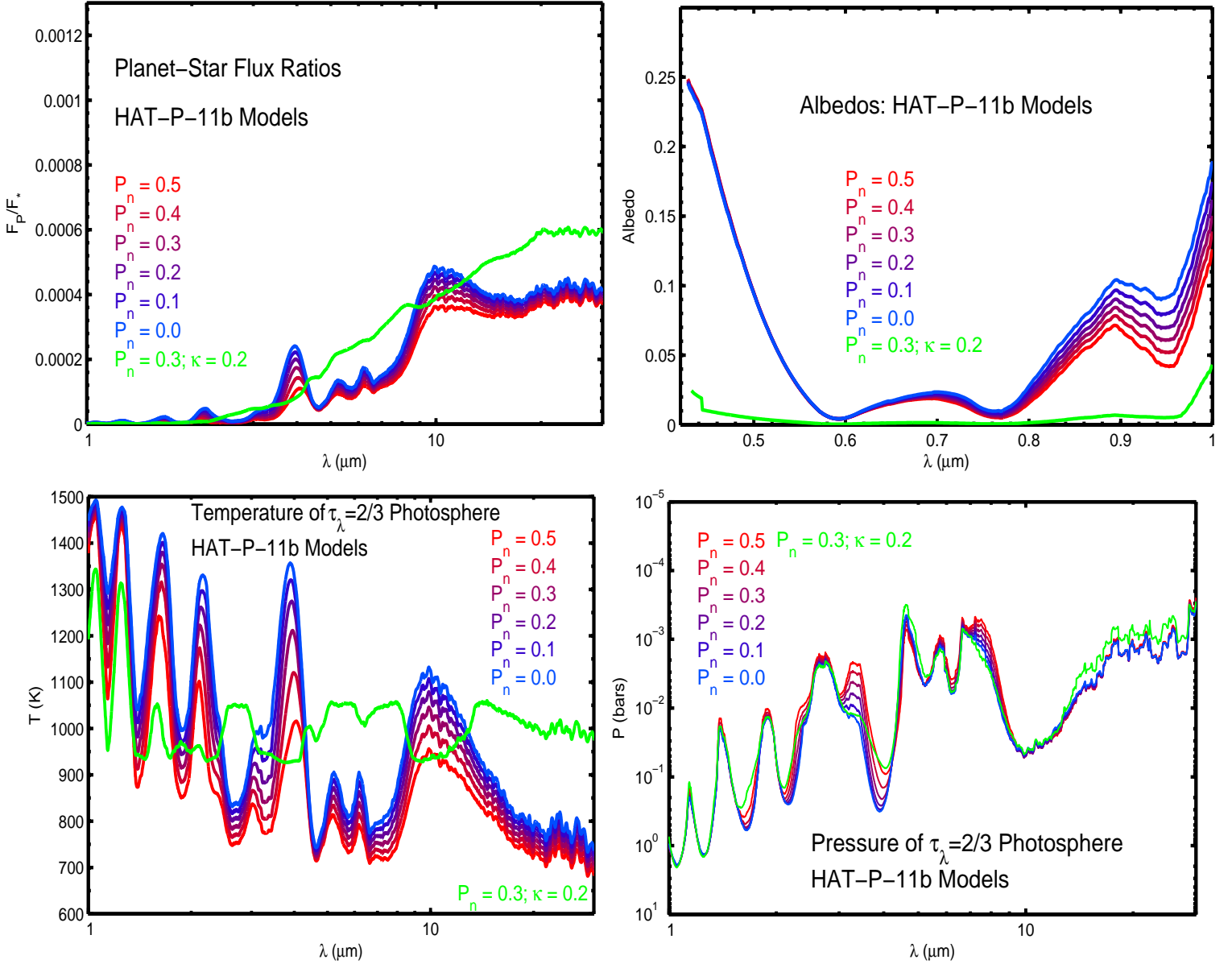


FIG. 3.— Additional characteristics of models of HAT-P-11b depicted in the bottom panel of Fig. 1. Completely analogous to Fig. 2.

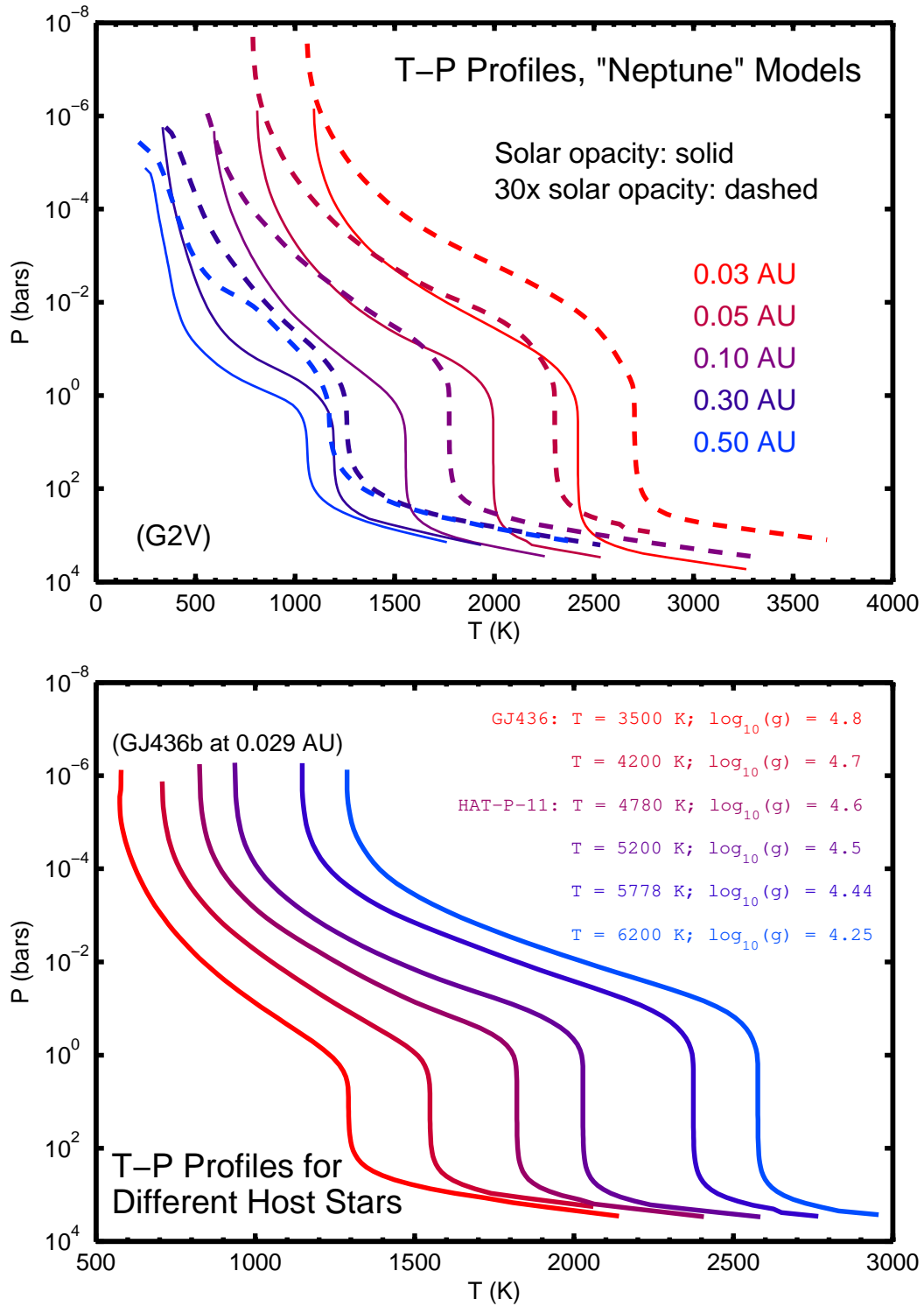


FIG. 4.— Model temperature-pressure profiles of GJ436b-like planet. In all models, the redistribution parameter $P_n = 0$. *Top*: Models are computed at a range of distances from a Sun-like star, at solar and at 30-times solar metallicity. More distant models are cooler, and more metal-rich models are warmer at a given pressure. *Bottom*: Models are computed for a range of host stars, from GJ436 (a cool M-dwarf) through an F9 star (6200 K).

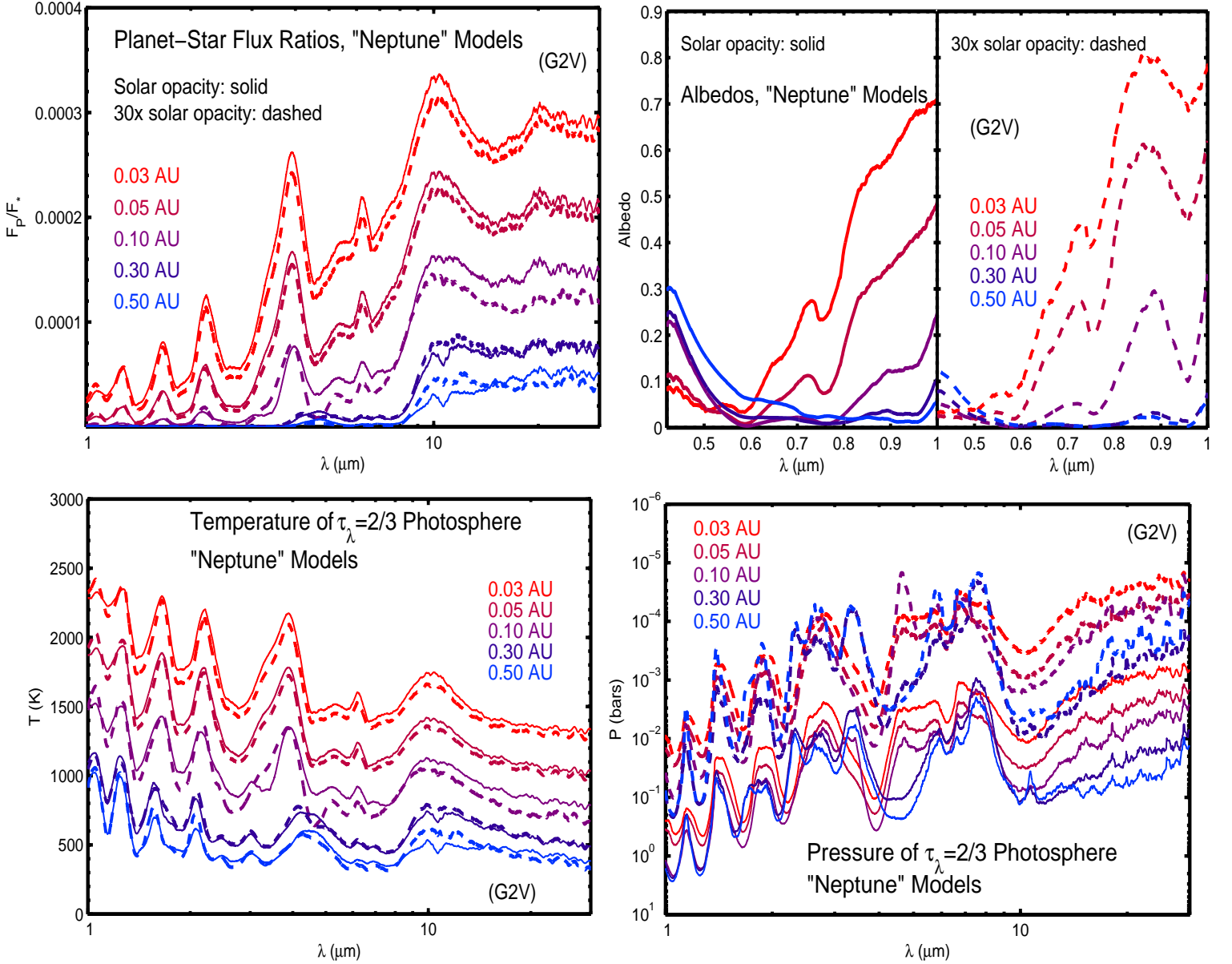


FIG. 5.— Additional characteristics of models for different orbital distances and metallicities depicted in the top panel of Fig. 4. Analogous to Fig. 2. *Top left*: Planet-star flux ratios for a GJ436b-like model planet at a variety of distances from a G2V star, at solar and at 30-times solar metallicity. Changes in metallicity have only a very modest influence on model spectra. *Top right*: Optical albedos for these same models. At high metallicity, generally the cooler, more distant models (dashed curves) have larger optical albedo. At solar metallicity, the albedo varies less smoothly with semimajor axis. *Bottom left*: Temperature of the $\tau_{\lambda} = 2/3$ surface, as a function of wavelength. *Bottom right*: Pressure of the $\tau_{\lambda} = 2/3$ surface, as a function of wavelength.

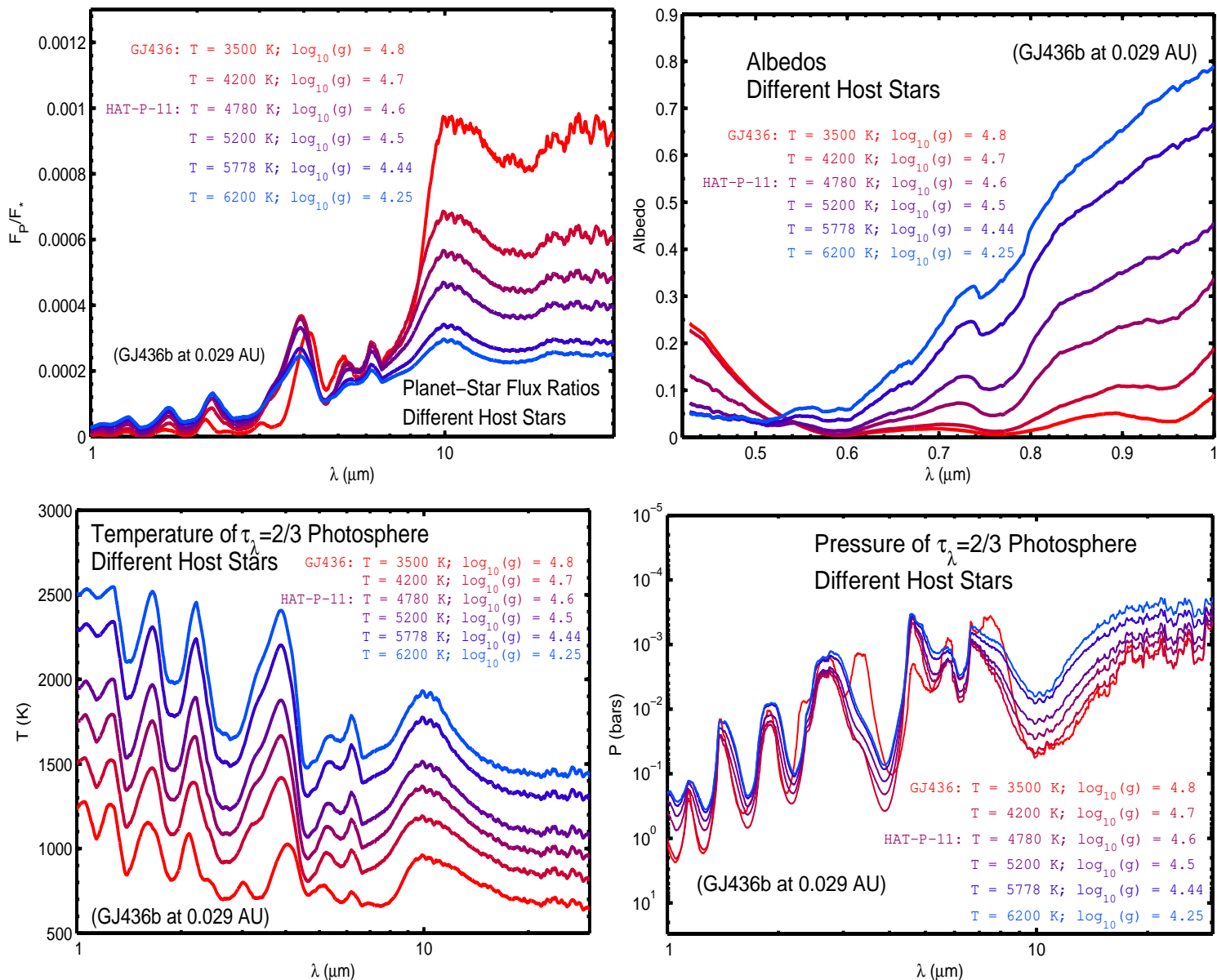


FIG. 6.— Additional characteristics of models for different host stars depicted in the bottom panel of Fig. 4. Analogous to Fig. 2.